Coupling local and global rf feedback loops for macroparticle tracking simulations

B. E. Karlsen-Baeck,[1,2,*] T. Argyropoulos,[2] J. Flowerdew,[2] L. Intelisano,[2] I. Karpov,[2] A. Lasheen,[2] and H. Timko[2]

[1]*Department of Physics, Sapienza Università di Roma, Rome, Italy*
[2]*CERN, CH-1211 Geneva 23, Switzerland*

(Received 24 September 2025; accepted 12 December 2025; published 10 March 2026)

Radio frequency (rf) control loops are vital components for the optimal operation of rf systems in synchrotron particle accelerators. Modeling these systems in macroparticle tracking simulations provides improved understanding of the complex interaction between the control loops, the beam-induced voltages in the rf cavities, and the circulating beam. This paper details an implementation of local and global rf control loops in the beam longitudinal dynamics (BLonD) simulation suite, which allow for the coupling of the two systems in a macroparticle tracking code for the first time. First, benchmarks of the local control loops in the CERN Super Proton Synchrotron (SPS) and Large Hadron Collider (LHC) are given. The implementation coupling the local and global loops is then tested in the SPS with momentum shifts at constant magnetic field and through the damping of phase offsets at injection into the LHC. Both test cases show the expected behavior and validate the model in BLonD. Finally, the SPS simulation model, which now is able to combine beam-induced voltages, global control loops and local ones, is benchmarked against measurements at the bunch-to-bucket transfer into the real accelerator. The simulations, using the coupled implementation of the loops, are able to reproduce bunch-by-bunch beam parameters at flat bottom as well as uncaptured beam generated at injection.

DOI: 10.1103/bxs4-f9nl

I. INTRODUCTION

Control loops are applied within a number of subsystems in synchrotron particle accelerators. The loops applied in the radio frequency (rf) systems [1] of these accelerators can be categorized into two main groups: global and local rf control loops. In this work, global feedback systems are defined as the control loops which regulate the global rf parameters, usually the rf frequency, of multiple rf systems in a synchrotron. An implementation of a global rf feedback system is present in all modern synchrotrons and usually consists of one or more control loops [2–8]. A classic example is the beam-phase loop (BPL), which regulates the rf frequency turn by turn such that the rf phase moves to the beam phase. It is used to damp coherent phase oscillations in the beam [9], reduce unwanted longitudinal emittance blowup due to rf background noise [10], and for controlled longitudinal emittance blowup [11]. In addition, a synchronization loop is commonly used to regulate the rf frequency to external references, e.g., to synchronize the rf systems of two accelerators [3,12]. For some accelerators, a radial loop is also applied, which gives rf frequency corrections based on the radial position of the beam [3,8]. Rf control loops which regulate the gap voltage in amplitude and phase of a single rf cavity will be referred to as local rf control loops. The purpose of these loops is to reduce the effective impedance of the fundamental mode of the rf cavities, regulate the rf gap voltage toward the desired setpoint, and linearize the rf amplification chain [13–16].

In most beam dynamics tracking suites, the rf parameters, namely the rf voltage V_{rf}, the rf phase ϕ_{rf}, and the rf frequency f_{rf}, are described as single constant values per rf system. More specialized suites allow the set of rf parameters for each rf system to change from one turn to the next [17–20]. The effect of global control loops, for example, is included by changing the rf frequency and rf phase from one turn to the next based on the simulated beam behavior. However, to include local control loops in tracking, the rf voltage and phase will change even within a turn.

Often, the action of local feedback systems is modeled as an effective impedance in beam dynamics simulations [21,22]. However, such models are typically applied assuming constant revolution and rf frequencies. This assumption no longer holds during bunch-to-bucket transfers of high-intensity beams in the presence of global rf control loops. At injection, the BPL is acting to damp out dipole oscillations due to injection errors in phase and

*Contact author: birk.beck@cern.ch

Published by the American Physical Society under the terms of the Creative Commons Attribution 4.0 International license. Further distribution of this work must maintain attribution to the author(s) and the published article's title, journal citation, and DOI.

energy and in doing so, is changing the rf frequency. To fully model the effect of the BPL, the effective impedance must also be dynamically updated turn by turn during the simulation, which can be computationally inefficient. Hence, self-consistent time-domain dynamic models of both local and global loops, as detailed in this paper, are essential to properly describe the complex behavior during the injection process. In particular, these models are necessary for precise studies of beam losses due to uncaptured particles and rf power limitations at injection into the Large Hadron Collider (LHC) [23] for the high luminosity (HL-)LHC era [24]. The very low tolerance for beam losses combined with the large beam loading due to the HL-LHC high-intensity bunch trains is expected to push the LHC rf system to its limit and require detailed studies at injection [25,26].

In the past, there have been attempts to dynamically change the effective impedance due to the local control loops at injection [27]. However, we go further by tracking the signal processing inside the local control loops while at the same time tracking the beam and the global loops. Implementing such simulation models poses a challenge because, in general, the rf frequency in the local control loops will no longer be an integer multiple of the revolution frequency as the global loops act. This causes a temporary phase slippage between the rf frequency, on which the local feedbacks act, and the revolution period of the beam. This is important because the revolution period, as we will see later, is often the basis of discretization in simulation. Furthermore, the local control loops will act back on the global loops through the rf cavity phase which is perturbed by the beam loading in the rf cavities.

In this publication, we show a novel approach to how both local and global rf control loops can be included in longitudinal beam dynamics simulations in a consistent way. The implementation of these models in the beam longitudinal dynamics (BLonD) simulation suite [28] is validated against measurements with various rf settings and bunch intensities in both the CERN Super Proton Synchrotron (SPS) and LHC. First, a description is given of how the feedback systems are modeled in BLonD (Sec. II) and benchmarks of the local feedback models are given (Sec. III). How these systems are coupled together in BLonD is described (Sec. IV) and test cases are provided to show how the implementation matches theoretical expectations (Sec. V). Finally, the coupling is benchmarked against measurements taken at the bunch-to-bucket transfer from the CERN Proton Synchrotron (PS) to the SPS (Sec. VI). The execution times of the simulations presented in this paper can be found in the Appendix.

II. INTERFACING RF FEEDBACK SYSTEMS WITH MACROPARTICLE TRACKING

The BLonD simulation framework has been used for this study. It contains benchmarked implementations of both global and local rf control loops [29–31]. Although the circuit model of the feedback is specific to each accelerator, the interface with the macroparticle tracking is generic and can be applied in other codes.

In BLonD, both the temporal position of the particle beam and the rf voltage, in phase and frequency, are described with respect to an external reference clock. The design time $t_d^{(n)}$ of this clock at turn n is defined as [28]:

$$t_d^{(0)} \equiv 0 \quad \text{and} \quad t_d^{(n)} \equiv \sum_{i=1}^{n} T_{\text{rev}}^{(i)} \quad \text{for } n \geq 1, \tag{1}$$

which is the accumulated revolution periods elapsed in the laboratory frame. Here $T_{\text{rev}}^{(n)}$ is the revolution period of the synchronous particle on the design orbit at turn n. The macroparticles are tracked through alternating energy kicks, e.g., from the rf cavities, and drifts around the magnetic lattice of the synchrotron. The time step of the particle motion at turn n for a given rf station is therefore the revolution period $T_{\text{rev}}^{(n)}$.

It is worth noting that the models implemented in BLonD only contain the feedback systems themselves and do not take into account effects like noise, for instance, from master oscillators. However, BLonD has a module for rf noise which can be used to include these imperfections on top of the feedback system models. In this paper, the beam is simulated for timescales short enough to neglect the effects of rf noise.

A. Global feedback implementation

The synchronous condition in a synchrotron is

$$\omega_{\text{rf},d}^{(n)} = h\omega_{\text{rev}}^{(n)}, \tag{2}$$

where the harmonic number h is an integer, and $\omega_{\text{rev}}^{(n)} \equiv 2\pi/T_{\text{rev}}^{(n)}$ is the angular revolution frequency. The design rf angular frequency, sometimes referred to as the open-loop frequency, is denoted as $\omega_{\text{rf},d}^{(n)}$. When the global rf control loops act, this condition no longer holds since they operate via frequency corrections in the rf system

$$\omega_{\text{rf}}^{(n)} = \omega_{\text{rf},d}^{(n)} + \Delta\omega_{\text{fb}}^{(n)}. \tag{3}$$

Here, $\Delta\omega_{\text{fb}}$ is the frequency shift due to the global feedback systems. In BLonD, the corresponding accumulated rf phase shift at turn n due to the shift in rf frequency is computed as

$$\Delta\phi_{\text{fb}}^{(n)} = \sum_{k=1}^{n} \left(\omega_{\text{rf}}^{(k)} - \frac{2\pi h^{(k)}}{T_{\text{rev}}^{(k)}}\right) T_{\text{rev}}^{(k)}. \tag{4}$$

The phase of the rf station with respect to the external reference clock $\phi_{\text{rf}}^{(n)}$ is therefore given as

$$\phi_{\mathrm{rf}}^{(n)} = \phi_{\mathrm{rf},d}^{(n)} + \Delta\phi_{\mathrm{fb}}^{(n)}, \tag{5}$$

with $\phi_{\mathrm{rf},d}^{(n)}$ being the design rf phase for turn n.

B. Local feedback implementation

In local rf control loops, also known as cavity controllers (CC), one common way of processing the signals is using in-phase (I) and quadrature (Q) components [4,32,33]. If these signals are processed digitally, the sampling can either be rf synchronous or at a fixed frequency. Currently, only CC models with rf synchronous sampling—an integer multiple of the rf period—are implemented in BLonD and will therefore be considered in this work. In principle, this scheme for coupling the global and local loops would also work for a fixed sampling frequency. In that case, careful resampling of the signals has to be performed and the phase slippage from one turn to the next has to be taken into account differently.

The implemented models use two sampling grids: the coarse and fine grids. The coarse grid is used to track the internal signal processing of the feedback system. The resolution of this grid is determined by the sampling chosen in the real system being modeled. In the SPS and LHC, for instance, the coarse-grid sampling period is 1 and 10 times the rf period, respectively. The fine grid is used to modify the kicks given to the macroparticles based on the calculations on the coarse grid and the cavity impedance. This is achieved by changing the rf wave in amplitude and phase bucket by bucket. The sampling time of the fine grid must therefore be sufficient to resolve the induced voltage and for this reason it has the same fine sampling as the longitudinal line density used in the simulation. The sampling is usually on the order of 64 to 256 samples per rf period for the SPS and LHC. The fine grid will therefore typically have a 64 to 2560 times higher sampling rate than the coarse grid.

When tracking with local control loops, the particles will receive an energy kick given by the voltage

$$V_{\mathrm{eff}}^{(n,k)} = |\boldsymbol{V}_{\mathrm{corr}}^{(n,k)}| V_{\mathrm{rf}}^{(n)} \sin\left(\omega_{\mathrm{rf}}^{(n)} \Delta t^{(n,k)} + \phi_{\mathrm{rf}}^{(n)} + \angle \boldsymbol{V}_{\mathrm{corr}}^{(n,k)}\right). \tag{6}$$

Here, $V_{\mathrm{eff}}^{(n,k)}$ is the effective voltage experienced by the particles at turn n and sample k on the fine grid. Please note that k will in general denote the sample number within a turn. Similarly, $\Delta t^{(n,k)}$ is the time offset with respect to the reference time $t_d^{(n)}$ along the turn, also on the fine grid. Furthermore, $\boldsymbol{V}_{\mathrm{corr}}^{(n,k)}$ is the sample-by-sample correction to the unperturbed gap voltage wave in the rf cavity given as

$$\boldsymbol{V}_{\mathrm{corr}}^{(n,k)} = \frac{\boldsymbol{V}_{\mathrm{gap}}^{(n,k)}}{\boldsymbol{V}_{\mathrm{set}}^{(n,k)}}, \tag{7}$$

with $\boldsymbol{V}_{\mathrm{gap}}^{(n,k)}$ and $\boldsymbol{V}_{\mathrm{set}}^{(n,k)}$ being the values at turn n and fine-grid sample k of the total gap voltage and the set point voltage, respectively. Note that $\boldsymbol{V}_{\mathrm{corr}}^{(n,k)}$, $\boldsymbol{V}_{\mathrm{gap}}^{(n,k)}$, and $\boldsymbol{V}_{\mathrm{set}}^{(n,k)}$ are complex numbers, signified by their bold lettering. It is important to note that $\boldsymbol{V}_{\mathrm{corr}}^{(n,k)}$ used in Eq. (6) includes the beam-induced voltage through $\boldsymbol{V}_{\mathrm{gap}}^{(n,k)}$ in Eq. (7). Hence, the beam-coupling impedance of the cavity is already included in the simulation through the local control loop model and should therefore not be introduced as an impedance source for other wakefield calculations. The induced voltage due to the impedance of all other accelerator components is tracked separately.

The rf beam current in I/Q used for the calculation of the gap voltage is [34]:

$$\boldsymbol{I}_{\mathrm{rf}}^{(n,k)} = -j2qN_p\lambda^{(n,k)} \exp\{j(\omega_{\mathrm{rf}}^{(n)} \Delta t^{(n,k)} + \phi_{\mathrm{rf}}^{(n)})\}, \tag{8}$$

where λ is the longitudinal line density normalized to 1, q is the particle charge, and N_p is the total number of real particles. This signal is initially computed on the fine grid because the induced voltage needs to be calculated over the line density of the beam. For the internal tracking of the feedback loops, this signal is downsampled to the coarse grid. The downsampling is achieved by summing the fine-grid samples in the rf bucket corresponding to the coarse-grid sample and consecutive rf buckets until the next coarse-grid sample.

Finally, the rf amplifier is treated as a current source driving the cavity. In the model, the generator current is used to derive the contribution to the gap voltage coming from the amplifier and to calculate the rf power demand if needed. The current is computed on the coarse grid by tracking the time-domain model of the local feedback system and is then interpolated to the fine grid. The specific way the generator current and beam current are used to calculate the total gap voltage used in Eq. (7) depends on the cavity type. The implemented feedback systems so far are the LHC superconducting standing-wave cavities and the SPS normal conducting traveling-wave structures (TWS) [35] along with their cavity feedback systems [30,31].

1. Superconducting standing-wave cavities in the LHC

For the case of superconducting standing-wave cavities ($Q_0 \gg Q_L$), such as in the LHC, the total gap voltage given in [34] can be calculated via the recursive equation

$$V_{\mathrm{gap}}^{(n,k)} = \left(1 - \frac{\omega_{\mathrm{rf}}^{(n)} T_s^{(n)}}{2Q_L} + i\Delta\omega^{(n)} T_s^{(n)}\right) V_{\mathrm{gap}}^{(n,k-1)} + (R/Q)\omega_{\mathrm{rf}}^{(n)} T_s^{(n)} \left(I_{\mathrm{gen}}^{(n,k-1)} - \frac{1}{2} I_{\mathrm{rf}}^{(n,k-1)}\right), \tag{9}$$

with the superscript k referring to the sample number along a turn n, I_{gen} is the generator current, T_s is the sampling

period, R/Q is the cavity geometry factor R upon Q, Q_L is the loaded quality factor, and $\Delta\omega = \omega_r - \omega_{\mathrm{rf}}$ is the detuning of the rf cavity, with ω_r being the resonant frequency of the cavity.

The LHC CC consists of a fast rf feedback and a one-turn delay feedback (OTDFB) [36]. The fast rf feedback has an analog high-pass branch and a digital low-pass branch in parallel. The time-domain model of the analog branch is given as

$$y^{(k)} = \left(1 - \frac{T_s}{\tau_a}\right) y^{(k-1)} + G_a(x^{(k)} + x^{(k-1)}), \tag{10}$$

with G_a and τ_a being the gain and delay of this branch. Furthermore, x is the input signal in I/Q and y the output signal. The digital branch is modeled as

$$y^{(k)} = \left(1 - \frac{T_s}{\tau_d}\right) y^{(k-1)} + G_a G_d e^{j\Delta\phi_{ad}} \frac{T_s}{\tau_d} x^{(k-1)}. \tag{11}$$

Here G_d and τ_d are the digital gain and delay, while $\Delta\phi_{ad}$ is the phase between the two branches.

Finally, the OTDFB is implemented as a comb filter with notches at the revolution frequency harmonics. The time-domain model used in BLonD is given as

$$y^{(k)} = \alpha_{\mathrm{comb}} y^{(k-N_{\mathrm{turn}})} + G_{\mathrm{OTDFB}}(1 - \alpha_{\mathrm{comb}}) x^{(k-N_{\mathrm{turn}})}, \tag{12}$$

where α_{comb} is the comb-filter coefficient, G_{OTDFB} is the OTDFB gain, and $N_{\mathrm{turn}} \equiv \lfloor T_{\mathrm{rev}}/T_s \rceil$ is one turn in number of samples on the coarse grid. The baseline parameters used inside the LHC CC throughout this paper, unless specified otherwise, are found in Table I.

2. Traveling-wave structures in the SPS

The main 200 MHz rf system of the SPS uses TWSs to give energy to the beam. The total gap voltage V_{gap} is given by

TABLE I. Baseline parameters in the LHC CC model.

Parameters	Symbol	Value
Cavity R upon Q	R/Q	45Ω
Loaded quality factor	Q_L	2.0×10^4
Overall loop delay	τ_{loop}	650 ns
Analog feedback delay	τ_a	170 μs
Analog feedback gain	G_a	6.79 μAV^{-1}
Digital feedback delay	τ_d	400 μs
Digital feedback gain	G_d	10
Analog-digital phase	$\Delta\phi_{ad}$	0
OTDFB gain	G_{OTDFB}	10
Comb-filter coefficient	α_{comb}	15/16

$$V_{\mathrm{gap}}^{(n,k)} = V_{\mathrm{gen}}^{(n,k)} + V_{\mathrm{beam}}^{(n,k)}, \tag{13}$$

i.e., the sum of the voltage induced by the generator, V_{gen} and the voltage induced by the beam, V_{beam}. The beam- and generator-induced voltages are calculated through a matrix convolution [16]

$$\begin{bmatrix} V_I(t) \\ V_Q(t) \end{bmatrix} = H * \vec{I} = \begin{bmatrix} h_s(t) & -h_c(t) \\ h_c(t) & h_s(t) \end{bmatrix} * \begin{bmatrix} I_I(t) \\ I_Q(t) \end{bmatrix}, \tag{14}$$

with H being the response matrix and I being the rf beam current or the generator current.

While the rf frequency changes by a non-negligible amount from the injection to the extraction energy, the SPS TWSs are not tunable and have a fixed central frequency. Frequency modulation is therefore applied to keep the response of the local feedbacks constant as the rf frequency, and consequently the carrier frequency, changes. The modulation is applied between the rf frequency and the TWS central frequency. The I/Q modulation from one arbitrary frequency ω_1 to another ω_2 can be done using the following transform:

$$\begin{bmatrix} x_{\mathrm{I},2}(t) \\ x_{\mathrm{Q},2}(t) \end{bmatrix} = M_{12}(t) \begin{bmatrix} x_{\mathrm{I},1}(t) \\ x_{\mathrm{Q},1}(t) \end{bmatrix}, \tag{15}$$

with $x_{\mathrm{I},1}$ and $x_{\mathrm{Q},1}$ being the I and Q components at the initial carrier frequency and $x_{\mathrm{I},2}$ and $x_{\mathrm{Q},2}$ the components at the final frequency. The matrix $M_{12}(t)$ describing the transformation can be expressed as

$$M_{12}(t) = \begin{bmatrix} \cos(\Delta\omega_{12} t + \phi_{\mathrm{m}}) & -\sin(\Delta\omega_{12} t + \phi_{\mathrm{m}}) \\ \sin(\Delta\omega_{12} t + \phi_{\mathrm{m}}) & \cos(\Delta\omega_{12} t + \phi_{\mathrm{m}}) \end{bmatrix}, \tag{16}$$

where $\Delta\omega_{12} = \omega_1 - \omega_2$, and ϕ_{m} is the turn-by-turn phase slippage between the two frequencies.

The SPS CC itself consists of an OTDFB and a feedforward (FFWD). The OTDFB is implemented in a similar way as the one in the LHC, while the FFWD is given as a finite-impulse response (FIR) filter with a gain G_{FFWD}. The taps of the FIR filter are designed to give a transfer function H_{FFWD} that satisfies

$$Z_{\mathrm{gen}}(\omega) H_{\mathrm{FFWD}}(\omega) \approx -Z_{\mathrm{beam}}(\omega), \tag{17}$$

where Z_{gen} and Z_{beam} are the TWS impedances toward the generator and beam, respectively.

III. BENCHMARKING THE LOCAL RF FEEDBACK SYSTEMS

The two local feedback models available in BLonD have both been benchmarked against measurements in the accelerators [30,31]. One of the benchmarks performed

was to recreate the injection of a 36-bunch train from the SPS into the LHC measured during a high-intensity test.

A. The bunch-by-bunch phase offsets at SPS top energy

The bunch intensity during the test was 1.8×10^{11} protons per bunch (p/b) at SPS flattop. The rf parameters in the SPS at extraction are found in Table II. The bunch-by-bunch intensities and bunch lengths were extracted from the measured longitudinal profiles of five injections. These parameters were then used, together with the SPS parameters in Table II, to create a macroparticle distribution in BLonD matching the measurement. The number of macroparticles was chosen to be around 1.2×10^6 per bunch, but varied for the bunches in the train according to their intensities. As was the case for the rest of the simulations in this paper, the number of macroparticles was chosen to give a sufficiently smooth beam line density.

The macroparticle distribution of the bunches is matched to their respective buckets via an algorithm [28]. This procedure is able to take into account both the distortion of the rf potential well caused by the impedance of the accelerator components and the variations in bunch length and intensity along the bunch train. However, it is not able to account for the bunch-by-bunch synchronous phase shift caused by the OTDFB in the SPS CC. The action of the CC is modeled as a linear scaling of the 200 MHz TWS impedance in the SPS impedance model used for the generation. In reality, the OTDFB will reduce the impedance in narrow notches at the revolution frequency harmonics. These notches have a single-sided bandwidth on the order of 100 Hz [16]. They would therefore require a very high resolution in frequency domain, and consequently a very long time domain array for the wakefield calculation. Hence, the macroparticles were tracked with the dynamic model of the SPS OTDFB instead. All other sources of beam-induced voltage in the SPS were calculated in frequency domain and tracked separately. The OTDFB parameters used during the measurements are also found in Table II.

TABLE II. Settings present in the SPS at extraction energy during the high-intensity test.

Parameters	Symbol	Value
Circumference	C	6911.5 m
Synchronous momentum	p_s	450 GeV/c
Transition gamma	γ_t	18
Harmonic number	h	4620
200 MHz rf voltage	$V_{\mathrm{rf},200}$	9.0 MV
800 MHz rf voltage	$V_{\mathrm{rf},800}$	1.35 MV
Relative phase of harmonics	$\Delta\phi$	π
200 MHz OTDFB gain	G_{OTDFB}	10
OTDFB comb-filter coefficient	α_{comb}	31/32
200 MHz FFWD gain	G_{FFWD}	0
Voltage partitioning	r_{part}	0.54

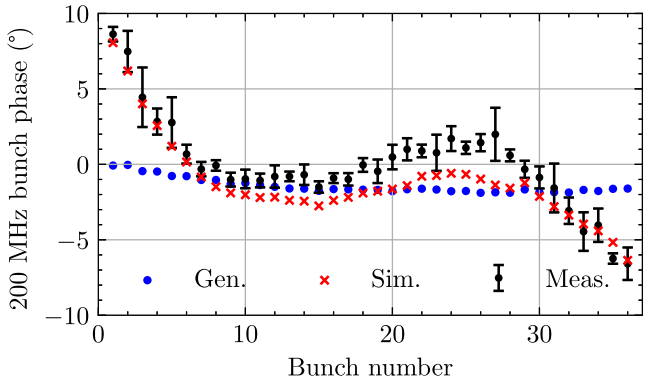

FIG. 1. Measured (black) and simulated (blue and red) 200 MHz bunch phases at SPS extraction to the LHC. The blue dots are the bunch phases before tracking at SPS flattop while the red crosses are after.

The 200 MHz bunch-by-bunch phase was extracted from the measurement as well as the line density from simulation. Figure 1 shows the bunch-by-bunch 200 MHz phase from measurement and simulation. The error bars in the measurement represent the standard deviation calculated from the bunch phase at extraction for each of the five 36-bunch trains that were injected into the LHC during the test. As expected, the bunches are equidistant when the macroparticle distribution of the train is generated using only the impedance model. However, after tracking the bunches for 1×10^4 turns with the SPS CC model, the phases are in excellent agreement with the measurement.

The combination of the distribution matching algorithm in BLonD and the dynamic model of the SPS CC enables the generation of very realistic macroparticle distributions of the bunch trains at SPS flattop.

B. Transients in rf power at LHC injection

The forward generator current was measured at the moment of injection of the 36-bunch train during the test and scaled to rf power. The dynamic model of the LHC CC in BLonD together with the macroparticle distribution discussed in Sec. III A was used to reproduce these measurements. Precise phase and energy matching was ensured during the test. The injection error in phase and energy was therefore assumed to be negligible. For this reason, the simulation did not include the action of the LHC global rf feedback system. The LHC parameters used in the simulation along with settings in the CC are found in Table III. A 12-bunch train, which was injected before the 36 bunches, was also tracked to make the rf power calculation more realistic. The simulation also included the full longitudinal impedance model of the LHC without the contribution from the rf system [21].

Figure 2 depicts the peak rf power turn by turn at the injection of the 36-bunch train. The blue shaded area represents the peak-to-peak spread in peak power for the

TABLE III. Settings present in the LHC at injection energy during the high-intensity test.

Parameters	Symbol	Value
Circumference	C	26658.883 m
Synchronous momentum	p_s	450 GeV/c
Transition gamma	γ_t	53.6
Harmonic number	h	35640
400 MHz rf voltage	V_{rf}	5 MV
Loaded quality factor	Q_L	2×10^4
Loop delay	τ_{loop}	650 ns
OTDFB gain	G_{OTDFB}	8
OTDFB comb-filter coefficient	α_{comb}	15/16
OTDFB complementary delay	τ_{comp}	1.05 μs
Analog fast rf feedback gain	G_a	1.02 $\mu\mathrm{AV}^{-1}$
Analog fast rf feedback delay	τ_a	170 μs
Digital fast rf feedback gain	G_d	10
Digital fast rf feedback delay	τ_d	400 μs

eight rf lines in beam 1, the clockwise rotating beam. Similarly, the red shaded area is the spread of the rf lines in beam 2, the counterclockwise rotating beam. The simulation, represented by the black line, shows close agreement with the transient in both beams. The simulation is on the lower side of the line-by-line spread, but this is expected since the maximum value is plotted. Furthermore, there is an estimated 20% error on the rf power reading as well as errors on the settings in Table III due to the way the rf system is commissioned, e.g., the feedback gains and loaded quality factor. Both error sources can contribute to why the peak power is slightly underestimated in simulation. Taking into account the sources of error, the LHC CC model is able to closely reproduce the dynamic interaction between the beam and the rf system at the bunch-to-bucket transfer.

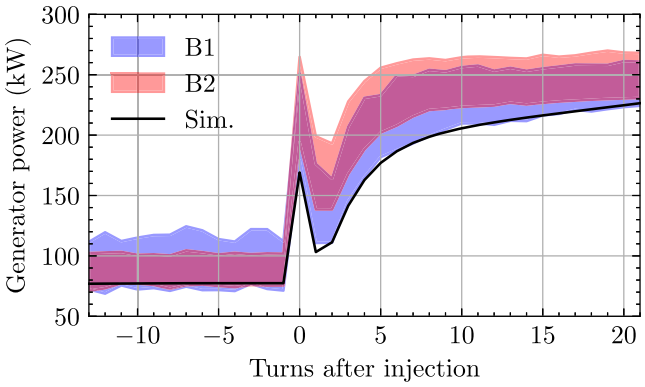

FIG. 2. Measured (black) and simulated (blue and red) generator forward power at injection into the LHC. The blue and red shaded areas correspond to the line-by-line spread in beam 1 and beam 2, respectively.

IV. COUPLING THE SYSTEMS AND IMPLEMENTATION

To couple the two types of feedback systems, one has to first consider the behavior of the local feedback when the condition in Eq. (2) no longer holds and the rf system is not synchronous with the design reference time. This will affect two important elements in the local feedback models, namely the modulation of the rf beam current and the position of the samples of the model during the turn.

First, the rf beam current calculation is considered. Figure 3 illustrates how the in-phase and quadrature components of the rf beam current change relative to the changing rf phase. When the bunch has an offset with respect to the bucket center (left) the modulation of the rf beam current is distorted. However, as the global rf loops act, the bucket is moved such that the bunch is in the bucket center and the I- and Q-components are changed accordingly (right).

To model the correct behavior of the rf beam current modulation, the rf frequency ω_{rf}, which enters in Eq. (8), must be updated turn by turn. Furthermore, the accumulated phase shift from Eq. (5) also modifies the rf beam current via the expression in the exponent in Eq. (8). Care must also be taken when performing the downsampling to the coarse grid, since this also has to be done synchronously with the rf clock.

Second, the internal sampling of the local rf loop models, the coarse grid, must be modified to keep the samples and rf bucket centers aligned in phase. Figure 4 shows how the rf buckets, and consequently the coarse grid, change with the effect of the global loops. The figure shows two cases for an rf system at $h = 4$. During the first turn, the synchronous condition is satisfied such that exactly four rf periods fit within one revolution period, and the same follows for the coarse-grid samples. However, at the second turn the frequency is changed and the condition in Eq. (2) no longer holds. This can be seen at the end of the second turn where a part of the last bucket is outside the turn. As the frequency changes turn by turn, the coarse grid has to expand or contract to stay synchronous with the rf wave and move due to the

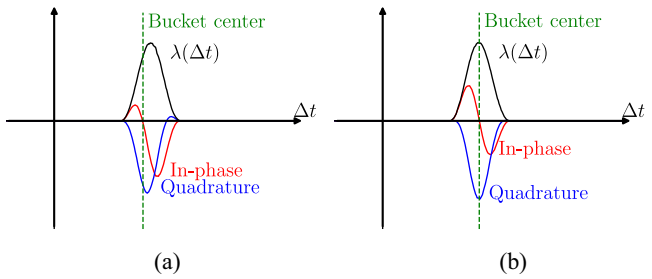

FIG. 3. rf beam current with the bunch off-center (a) and centered (b) with respect to the rf bucket.

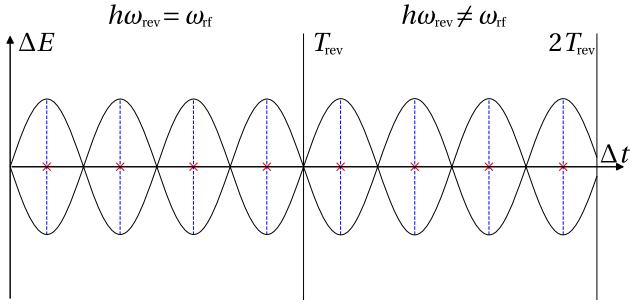

FIG. 4. Change in sampling position in time from one turn to the next when the rf frequency goes from $h\omega_{\mathrm{rev}} = \omega_{\mathrm{rf}}$ to $h\omega_{\mathrm{rev}} \neq \omega_{\mathrm{rf}}$. The red markers indicate the position of the samples of the cavity loop in time while the blue dashed lines represent the rf bucket centers.

accumulated phase shift. In simulations, this was implemented by changing the sampling period T_s according to the rf period as

$$T_s^{(n)} = \frac{2\pi n_s}{\omega_{\mathrm{rf}}^{(n)}} \tag{18}$$

with n_s being the ratio between the rf frequency and the sampling frequency. The partial rf bucket at the end of the current turn is computed and added to the next turn

$$\Delta T^{(n)} = -\frac{\phi_{\mathrm{rf}}^{(n)}}{\omega_{\mathrm{rf}}^{(n)}}. \tag{19}$$

As a consequence of these shifts, the sampling time $t_s^{(n,k)}$ on the coarse grid can be expressed as

$$t_s^{(n,k)} = \left(k - 1 + \frac{1}{2n_s}\right) T_s^{(n)} + \Delta T^{(n)}. \tag{20}$$

The detected phase of the cavity gap voltage changes dynamically as well due to beam loading, which depends on the local control loops, and must therefore be taken into account in the model. Global control loops, such as the BPL, need the phase of the total vector sum of the gap voltages in the cavities to compare with the beam phase for regulation. The phase error $\Delta\phi_{\mathrm{BPL}}^{(n)}$ at turn n used for regulation by the BPL is therefore given as

$$\Delta\phi_{\mathrm{BPL}}^{(n)} = \frac{1}{N_b}\sum_{i=1}^{N_b}\left(\angle\left\{\sum_{l=1}^{n_{\mathrm{cav}}} V_{\mathrm{gap}}^{(n,l)}(\Delta t_{\mathrm{beam}}^{(n,i)})\right\} - \phi_{\mathrm{beam}}^{(n,i)}\right). \tag{21}$$

Here, N_b is the number of circulating bunches, n_{cav} is the number of cavities on the frequency that the BPL is regulating, $\Delta t_{\mathrm{beam}}^{(n,i)}$ is the longitudinal position in time w.r.t. $t_d^{(n)}$ of bunch i, and $\phi_{\mathrm{beam}}^{(n,i)}$ is the phase of bunch i. As is commonly done in real rf systems, the beam phase $\phi_{\mathrm{beam}}^{(n,i)}$ is derived by integrating the rf component of the beam line density, which is usually measured by some pickup along the ring. Any noise occurring from this procedure can therefore be treated in the same way in these simulation models as is done in the hardware of a real rf system.

V. TESTING THE IMPLEMENTATION

To check the correct implementation of the interaction between the control loops, two tests were conducted. Namely, a check that the local loops work with deviations from the design orbit and that steady state can be recovered from transient states using the global loops. Note that, for simplicity, beam-induced voltages from other impedance sources were not included for these tests.

A. Cavity feedback regulation with deviations from the design orbit

As introduced in Sec. II, the simulation suite BLonD uses a coordinate system, which is defined with respect to the design orbit and the synchronous energy of the synchrotron. The time step, and hence the BLonD reference frame, is therefore locked to the design revolution period clock. If the rf frequency of the accelerating system is no longer an integer multiple of the revolution period, the rf system will decouple from the reference frame, and the rf buckets will slip in phase as described by Eq. (4). The local feedback systems in BLonD act synchronously with the rf wave in the cavities and will therefore be independent of the reference frame. The implementation of the coupling should enable the local feedback systems to act in the same way even when the rf system phase is slipping.

To test this, simulations with the beam and rf parameters in the SPS with different momentum offsets were performed to verify that the regulation of the 200 MHz CC model [16,30,37] would be invariant with respect to the rf phase slippage. The parameters chosen for this test are close to the baseline specifications for the SPS at extraction energy during the HL-LHC era. A 36-bunch train with a bunch intensity of 2.3×10^{11} p/b giving a peak rf beam current of 2.62 A was considered for this test. All bunches had the same longitudinal distribution and intensity and were all modeled with 1×10^5 macroparticles, i.e., 3.6×10^6 macroparticles in total. This bunch train was tracked including the model of the OTDFB and FFWD at a beam momentum of 450 GeV/c with an rf voltage of 10 MV in the 200 MHz rf system and 1 MV in the 800 MHz rf system. The relative phase between the two rf systems were such that they were in phase at the bunch position. Three cases were simulated, with no rf frequency offset and with ± 2 kHz offsets. The frequency offsets correspond to momentum offsets of ± 1.46 GeV/c, which is more than 3 times the rf bucket height of 450 MeV/c. Figure 5 depicts

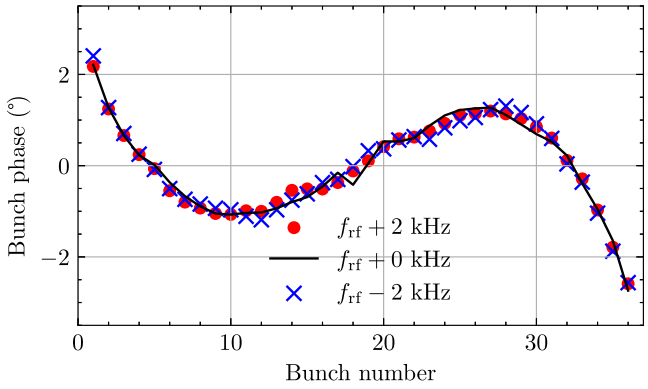

FIG. 5. Bunch-by-bunch phase offset for a bunch train slipping in the SPS due to an rf frequency offset of 2 kHz (red), 0 kHz (black), and −2 kHz (blue).

the bunch-by-bunch phase offset for the different cases after tracking for 10^4 turns. Indeed, the effect of the CC regulation is the same even when the rf phase slips forward or backward with respect to the reference frame. The small differences depicted in Fig. 5 can be attributed to small oscillations in the bunches due to the initial turn-by-turn phase slippage and the initial transient due to the action of the CC.

The same simulation was also run for intermediate frequency offsets. Figure 6 shows the average bunch-by-bunch phase error with respect to the no-offset case. The error, $\varepsilon_{\phi_{\mathrm{beam}}}$, was estimated as

$$\varepsilon_{\phi_{\mathrm{beam}}} = \frac{1}{N_b(\phi_{\mathrm{beam}}^{\mathrm{pk\text{-}pk}})^2}\sum_{i=1}^{N_b}(\phi_{\mathrm{beam}}^{(i)} - \phi_{\mathrm{beam,0\ kHz}}^{(i)})^2 \qquad (22)$$

with $\phi_{\mathrm{beam}}^{\mathrm{pk\text{-}pk}}$ being the peak-to-peak phase offset of the bunch train and $\phi_{\mathrm{beam,0\ kHz}}^{(i)}$ the phase offset pattern without a frequency shift. The average error was found to be between 2% and 3% and does not correlate with increasing offsets, see Fig. 6. The error is small enough to stem from dipole oscillations excited at the start of the simulations.

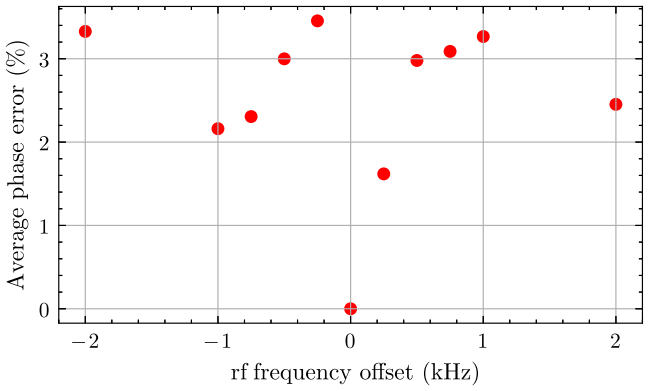

FIG. 6. Average bunch-by-bunch phase error with respect to no frequency offset.

The beam had the same behavior in all cases, and one can conclude that the action of the local loop is invariant as the rf system and beam slip relative to the external reference clock. More specifically, the expression for the sampling in Eq. (20) correctly takes into account offsets from the design rf frequency $\omega_{\mathrm{rf},d}$ and how the samples slip in time with respect to $t_d^{(n)}$.

B. Damping turn-by-turn transients

One of the applications of the BPL is to damp dipole oscillations of the bunches, e.g., caused by injection errors in phase or energy at a bunch-to-bucket transfer. This effect can be observed in additional rf power requested by the control loop action and on the beam itself. The recovery from transient conditions at injection to steady state was analyzed for a 36-bunch train simulated at injection into the LHC while tracking the LHC CC model. The beam control is also implemented in BLonD for this accelerator [29] and was tracked as well. The bunch train was simulated at the injection momentum, 450 GeV/c, with a bunch intensity of 1.6×10^{11} p/b, an initial bunch length of 1.2 ns, and an rf voltage of 5 MV, which is close to the parameters used during LHC operation in 2024. The number of macroparticles used per bunch to model the beam was 1×10^5 for these simulations.

Four cases were simulated with the same initial particle distribution; with the BPL open and closed and with a 0° and 40° initial phase offset. Simulating with and without the BPL when the phase offset is zero should result in exactly the same beam and rf system behavior. The turn-by-turn evolution in mean bunch length of the train is shown in Fig. 7(a). As expected, the bunch length is preserved and approximately constant when the BPL is closed, even with an initial phase offset as large as 40°. When the BPL is open, however, the bunch length oscillates significantly due to the nonrigid dipole motion excited by the initial phase error. This is also reflected in the turn-by-turn peak power plotted in Fig. 7(b). Due to the initial offset, extra transients in the rf power occur, even with the BPL closed. The zero-offset cases and the ones with the BPL closed converge to the same steady-state peak power, reflecting the correct regulation of the BPL. The mismatched case without the BPL action has a longer-lasting transient in rf power. Due to the bunch lengthening caused by the mismatch, this scenario also settles to a lower peak power.

Both the global control loops and the rf beam current calculation in the local loops calculate the phase of the beam relative to the rf system. Figure 8 shows the turn-by-turn phase evolution as estimated from the rf beam current (black) and the LHC BPL model (red). The frequency of the bunch phase oscillations for the case with the BPL open correspond to the synchrotron frequency. The oscillation of the bunch phase with the BPL closed, however, is

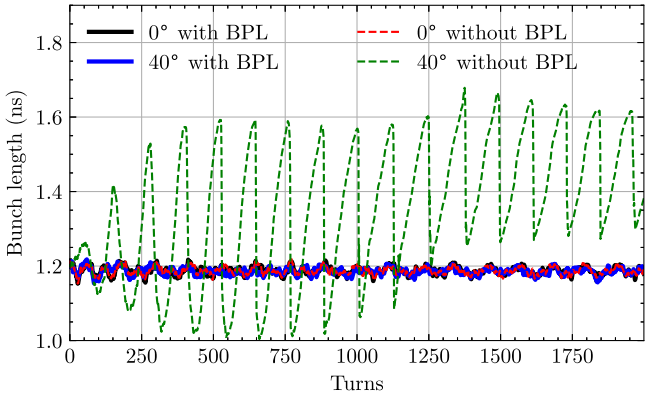

(a)

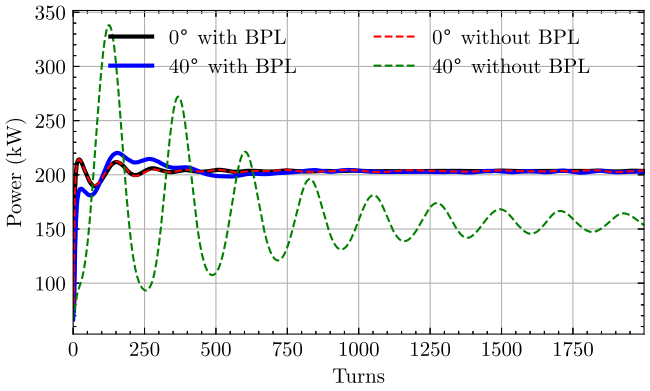

(b)

FIG. 7. Simulation of a 36-bunch train at injection into the LHC with the BPL (black) and without (red). Furthermore, a simulation of the same train with a 40° phase kick with BPL (blue) and without (green). Turn-by-turn average bunch length of the train during the first 2×10^3 turns is shown in (a) and the corresponding turn-by-turn peak rf power is shown in (b).

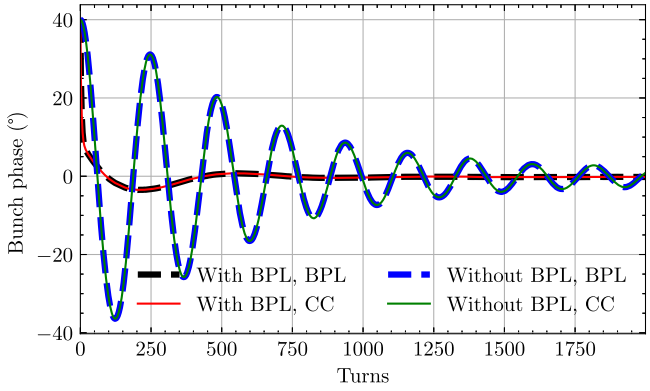

FIG. 8. Simulated turn-by-turn average bunch phase at injection calculated by the BPL and CC models. The phase calculated from the rf beam current in the CC is represented by the red and green lines when the BPL is closed and open, respectively. The black and blue lines correspond to the phase calculated by the BPL model when the BPL is closed and open, respectively.

dominated by the damping due to the BPL regulation. Indeed, the two loops compute exactly the same beam phase. The error between the two phase estimates was also analyzed turn by turn for the different initial phase offsets. The relative error between the estimates was found to be on the order of 10^{-11}, which is down to floating point precision.

This test shows that the two calculations agree on when the beam arrives to the rf station relative to the rf wave. Additionally, it confirms that the phase term in Eq. (8) correctly takes into account the action of the global loops.

VI. BENCHMARKING INJECTION TRANSIENTS DURING BEAM TRANSFER TO THE SPS

As a final benchmark, measurements at injection into the SPS during a machine development (MD) session were analyzed and reproduced in simulation using the coupled-loop implementation. Trains of 72 bunches with 2.6×10^{11} p/b, the nominal bunch intensity at SPS injection for HL-LHC [38], were injected from the PS while varying the injection phase offset from −40° to 40°.

A. Injected beam parameters

The line density of the beam was measured during the first 1500 turns for 13 of the trains extracted from the PS during the MD session. The full width at half maximum bunch lengths were derived at the first turn for all the injections from the PS. The bunch lengths were then scaled to the 4σ Gaussian equivalent by applying

$$\tau_b = \frac{2}{\sqrt{2\ln 2}} \tau_{\mathrm{FWHM}}. \tag{23}$$

Similarly, the relative bunch intensities were extracted by integration of the profile of each bunch. The bunch profiles were also used to compute the spread in bunch-by-bunch phase offsets. The mean (black line) and standard deviation (gray shaded area) across the 13 measured injections in intensity and bunch length for each of the 72 bunches are illustrated in Fig. 9. The mean length and intensity bunch by bunch were used to generate a representative macroparticle distribution for each bunch in the train for the simulations.

To fit into the 5 ns SPS bucket, the bunches in the PS are rotated with a nonadiabatic voltage jump at extraction [39,40]. Due to the decreasing synchrotron frequency near the edge of the buckets, the rotation distorts the tails of the beam distribution at extraction. To obtain a realistic macroparticle beam distribution in energy and time, the rotation process was simulated at PS flattop with the beam parameters that were found in measurement. The bunches were generated before the bunch rotation, assuming a binomial distribution [41]

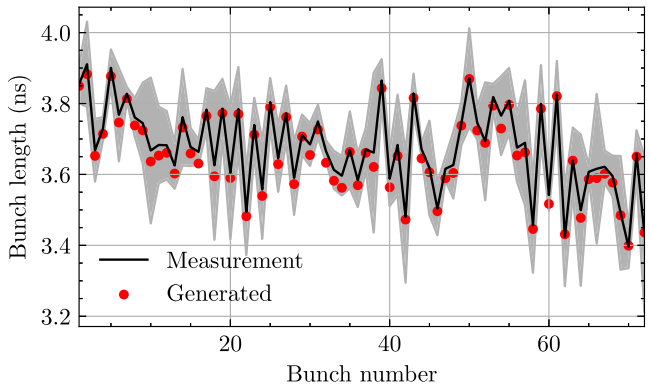

(a)

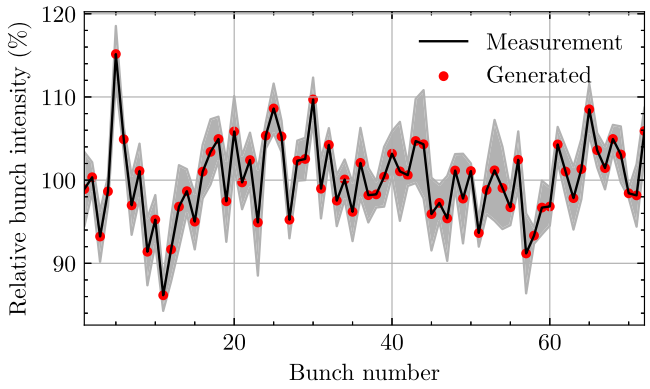

(b)

FIG. 9. Average measured beam parameters (black line) with the standard deviation of these parameters (shaded area) plotted with the generated macroparticle distributions (red dots). The bunch length of the 72 injected bunches is shown in (a) and their bunch intensity, relative to 2.6×10^{11} p/b, is shown in (b).

$$\mathcal{F}(\mathcal{H}) = \mathcal{F}_0 \left(1 - \frac{\mathcal{H}}{\mathcal{H}_{\max}}\right)^{\mu}, \tag{24}$$

which is often used in CERN synchrotrons to describe the longitudinal distribution of proton bunches. In the equation, $\mathcal{F}_0$ is a normalization factor, $\mathcal{H}$ is the Hamiltonian value, and $\mathcal{H}_{\max}$ is the Hamiltonian value along the phase-space trajectory enclosing all the particles in the bunch. The binomial exponent μ was assumed to be 1.5 based on previous observations in the PS and originates from the way the beam is produced in the preinjectors.

The beam profiles were, however, only measured at injection into the SPS. To generate the macroparticle distribution before the voltage jump in the PS, the procedure was therefore to scale the length of the bunches such that they would match the measured bunch lengths, depicted in Fig. 9(a) (black lines), after the simulated rotation. Each bunch was matched to its rf bucket using the parameters in Table IV before the voltage jump while taking into account the variations in bunch length and intensity. Around 1×10^6 macroparticles were used per bunch with the exact amount for each bunch varying according to the intensity variation along the trains. The macroparticles were then tracked for 143 turns with the voltage program illustrated in Fig. 10. Note that the voltages used in the simulation were lower than the nominal voltage in [39] because correction factors from beam-based rf voltage calibration were taken into account. The relative phase between the two harmonics was such that they were in phase at the bunch position. The resulting beam parameters of the macroparticle distributions at injection into the SPS, including the bunch rotation, are summarized in Fig. 9. Finally, the spread in phase of the different bunches was recreated by shifting each of the generated bunches by their respective measured offsets.

TABLE IV. Parameters in the PS for the studies at injection into the SPS.

Parameters	Symbol	Value
Circumference	C	628.3 m
Synchronous momentum	p_s	25.92 GeV/c
Transition gamma	γ_t	6.1
Harmonic number	h	84
40 MHz rf voltage, before rotation	$V_{\mathrm{rf,i,40}}$	73.3 kV
40 MHz rf voltage, after rotation	$V_{\mathrm{rf,f,40}}$	500.4 kV
80 MHz rf voltage, before rotation	$V_{\mathrm{rf,i,80}}$	0
80 MHz rf voltage, after rotation	$V_{\mathrm{rf,f,80}}$	589.1 kV
Relative phase of harmonics	$\Delta\phi$	π

B. Beam behavior during filamentation

Simulations at SPS injection were performed with the generated PS beam distributions. The parameters of the SPS and the settings present in the rf system during the measurements can be found in Table V. The first 1500 turns in the SPS were tracked using a model of the SPS beam controller [7] and the SPS CC [16], with the OTDFB closed. These simulations also included the full model of the longitudinal impedance of the SPS, but without the

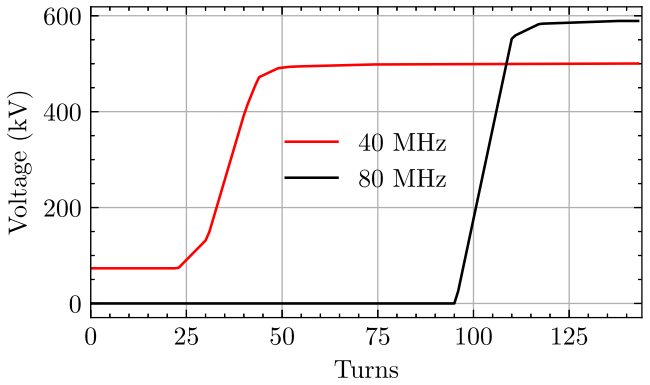

FIG. 10. Voltage amplitude of the 40 MHz (red) and 80 MHz (black) rf systems in the PS during the bunch rotation.

TABLE V. Parameters in the SPS for the studies at injection.

Parameters	Symbol	Value
Circumference	C	6911.5 m
Synchronous momentum	p_s	25.92 GeV/c
Transition gamma	γ_t	17.95
Harmonic number	h	4620
200 MHz rf voltage	$V_{\mathrm{rf},200}$	4.48 MV
800 MHz rf voltage	$V_{\mathrm{rf},800}$	0.45 MV
Relative phase of harmonics	$\Delta\phi$	π
200 MHz OTDFB gain	G_{OTDFB}	20
OTDFB comb-filter coefficient	α_{comb}	63/64
Voltage partitioning	r_{part}	0.52

contribution from the 200 MHz rf system. The FFWD in the SPS CC was disabled for simplicity during these measurements. For comparison, identical simulations were performed with a simplified model of the effect from the CC, i.e., with the static 200 MHz TWS impedance reduced by a factor 20, instead of including the dynamic SPS CC model.

The filamented bunch lengths were studied in measurement and simulation. Figure 11 shows a comparison of the bunch length after filamentation. Since the length of the bunches was oscillating after the 1500 measured turns, the filamented bunch length was estimated by computing the average bunch length from turn 1400 to turn 1500. The bunch length after filamentation is well reproduced in simulation, even recreating the bunches becoming shorter from the head to tail of the bunch train. The simplified model gave a more uniform bunch length across the train. In general, the simplified model also gave longer bunches after filamentation compared to the dynamic one, while the measured values were found to be in between.

The evolution of the bunch-by-bunch phase was analyzed with the same method for both the measurements and the simulations. Figure 12 shows the steady-state 200 MHz

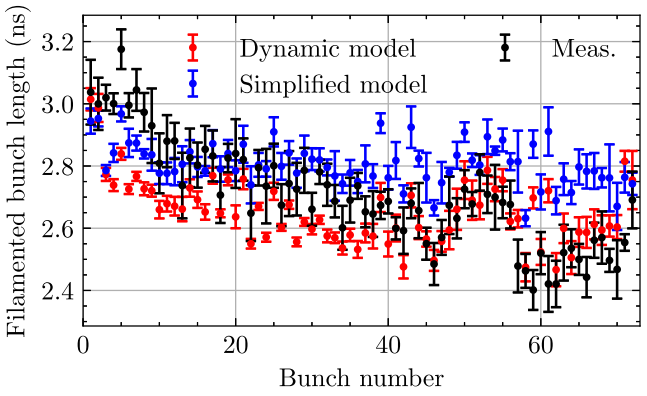

FIG. 11. Simulated (red and blue) and measured (black) bunch length averaged over turns 1400 to 1500 (dots). Every profile measured during the MD was used to find the mean and standard deviation. Simulations were run both with the dynamic model (red) and the simplified one (blue).

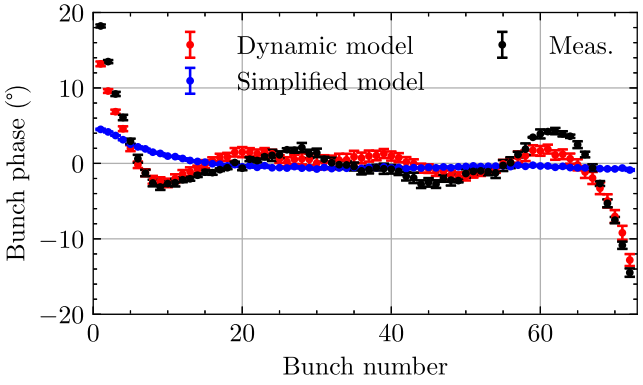

FIG. 12. Measured (black) and simulated (red and blue) average bunch phase offsets from turn 1000 to turn 1500 after injection. The red points represent the simulation result using the dynamic SPS CC model while the blue was produced using the static scaling of the TWS impedance.

phase offset for each of the 72 bunches. The bunches were still oscillating in phase after the 1500 turns measured. The steady-state phase offsets were therefore estimated by averaging the bunch phase from turn 1000 to 1500 for each bunch. These bunch-by-bunch values were then averaged over the 13 different injections that had profile measurements. The injection phase for these measurements ranged from −53° to 32°. The error bars in the plot represent the standard deviation over the 13 measurements. The same data treatment was done for the simulated data. The simulations using the simplified impedance model are not able to reproduce the steady-state offset observed in the measurements. In contrast, the dynamic model displays excellent agreement with the measurement.

Figure 13 (top) shows the maximum phase deviation from the measurements and simulation as the bunches oscillate after injection. The maximum deviation was derived with respect to the steady-state bunch phase shown in Fig. 12. This excursion was calculated for each bunch of the 13 measured beam profiles at injection and averaged over to produce the values represented by the black dots in the plot. The bars in the plot are the standard deviations of the excursion over the measurements. The same was done for the simulations using the dynamic model of the SPS CC (red dots) and with the static scaling of the TWS impedance (blue dots).

One can see from Fig. 13 (top) that the simulations using the dynamic model reproduce the bunch-by-bunch variation of the phase oscillation amplitude very well. The large oscillations excited toward the head and tail of the bunch train are caused by the variation in the rf phase imposed by the OTDFB (see Fig. 12). In comparison, the simplified impedance model of the TWS does not reproduce this behavior because the bunch-by-bunch phase shift caused by the OTDFB is not present. The result is that the simplified case gives a uniform oscillation amplitude across the bunch train and underestimates the overall amplitude of the oscillations.

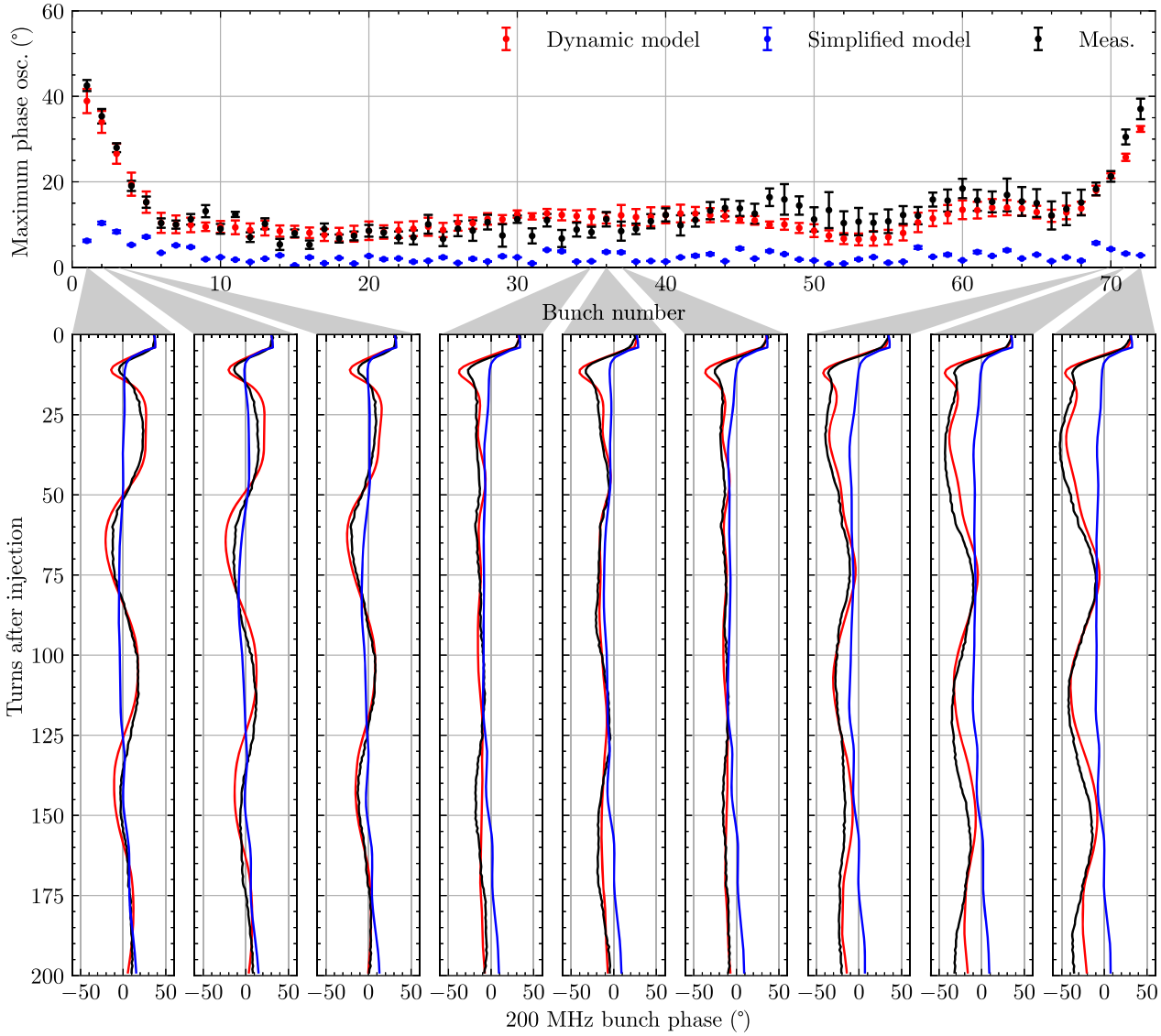

FIG. 13. Measured (black) and simulated (red and blue) phase oscillations at injection into the SPS. The top plot shows the maximum oscillation amplitude for each bunch across the phase error scan. The bottom plots show the bunch phases oscillations at injection due to a phase error of 32° and a 10 MeV energy error. The bunches plotted are 1, 2, 3, 34, 35, 36, 70, 71, and 72 from left to right. In all plots, the red color indicates simulations with the dynamic SPS CC model while the blue represents the ones using the scaled TWS impedance.

Figure 13 (bottom) depicts the phase oscillation of nine of the 72 bunches in the train for the first 200 turns for a specific set of injection errors in phase and energy. The injection phase error, derived from the bunch phase, was 32°, while an energy error of 10 MeV was found to most closely reproduce the overall behavior in the measurements. The BPL, in the SPS beam controller, is switched on after the first five turns. This is done because the strong beam loading in the 200 MHz system at injection heavily perturbs the cavity vector sum sent to the BPL. After the fifth turn, the BPL tries to correct the injection phase offset, which takes another five turns. The measurements (black) and simulations using the dynamic model (red) are in excellent agreement for all bunches shown in Fig. 13 (bottom). For reference, the simplified model (blue) displays a very different behavior. The bunches oscillate to a lesser extent and the overshoot in bunch phase around turn 10 is not present.

The remaining error observed in simulation using the dynamic model, in particular the slippage in the phase of the bunch phase oscillations, is likely due to the way the macroparticle distributions were generated for tracking. Only one beam distribution for a given tail population was generated for tracking, see Fig. 9. In reality, there was a spread in both bunch length and intensity from the PS from cycle to cycle during the measurement session (indicated by the gray shaded areas in Fig. 9). Hence, the specific intensity and distribution of the measured bunches in

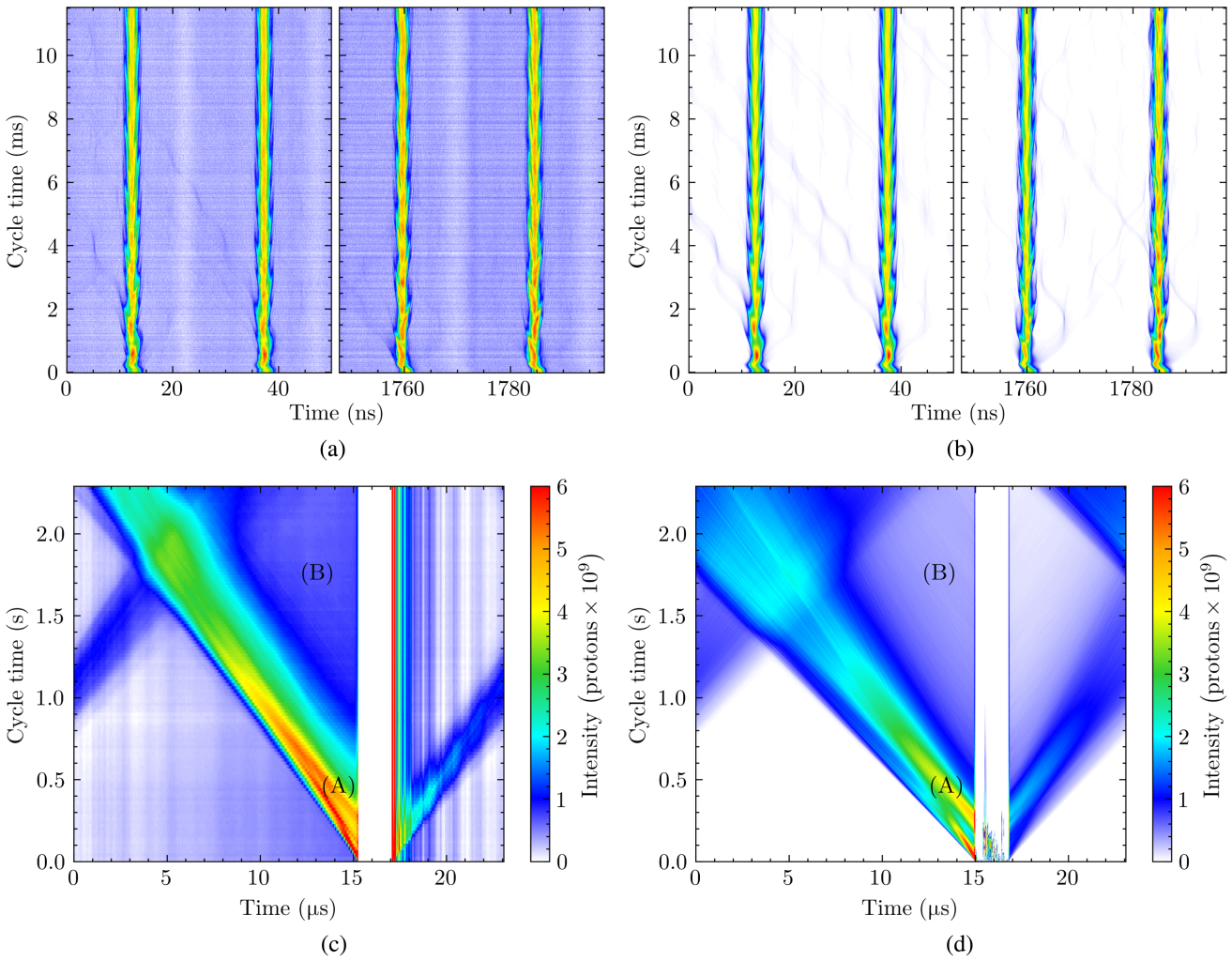

FIG. 14. Bunch profiles at injection measured by the wall current monitor (a) and from simulations (b). The left and right frames of each subplot are the two first and last bunches in the train, respectively. The uncaptured beam circulating at injection energy as measured by the FBCT (c) and from simulation (d) is also shown.

Fig. 13 are not exactly the same as those of the simulations. Missing contributions in the longitudinal impedance model of the SPS are expected to be small [42,43]. It is therefore unlikely that the lower synchrotron frequency observed in measurement is caused by potential-well distortion. Furthermore, the rf voltage in the SPS is calibrated with beam at the start of each year during beam commissioning [44]. Although small drifts in voltage have been observed during yearly runs in the past, it is likely negligible. Taking into account the sources of error, the final simulated bunch-by-bunch phase offset is in very good agreement with the measurement. This was found to be the case for all configurations, as summarized in Fig. 13 (top).

C. Simulating uncaptured beam at SPS flat bottom

At injection into the SPS, some particles end up outside the rf buckets and circulate with a momentum offset compared to the bunched beam. These particles constitute the uncaptured beam and have also been studied in the past in the context of PS-to-SPS beam transfer [45]. Figure 14(a) shows the measured bunch profiles for the first 11.5 ms after injection. Uncaptured beam, represented as dark blue lines, generated by the injection oscillations can be observed next to the bunches as they circulate.

Figure 14(b) depicts the bunch profile evolution for a simulated injection using the dynamic model of the SPS CC and the same initial phase offset as in the measurement, approximately 32°. The injection oscillations of the bunches are well reproduced, similarly to the reconstructed bunch phase plotted in Fig. 13. The uncaptured beam is very clearly visible in simulation for all the bunches shown in Fig. 14(b). Both the generated uncaptured beam and how it drifts away from the bunches agree very well with the measurement [Fig. 14(a)]. Considering for instance the second bunch in the train at around 35 ns [Fig. 14(b)], two groups of uncaptured particles can be observed leaving the

bunch at around 1 and 2 ms after injection and then arriving progressively earlier turn by turn due to their lower energy. Such uncaptured particles are indeed also present for the measured bunch in Fig. 14(a).

The beam intensity was measured using the fast beam current transformer (FBCT) during the MD session. The FBCT is able to measure the amount of beam for each 25 ns slot of the turn. The measurement was used to compute the uncaptured beam drifting away from the bunch train, which is illustrated in Fig. 14(c). To generate the plot, the turn-by-turn ripple in the baseline of the measurement was corrected for by subtracting the values in each turn by its minimum value. The intensity of the main bunches, which can be seen at around 15 to 17 μs, was then set to zero for each turn in order to only see the uncaptured beam. As shown in Fig. 14(c)(A), most of the uncaptured beam drifts away from the bunch train after the first 500 ms.

The equivalent simulation is represented in Fig. 14(d). The simulation reproduces the measurement very well. Again, one can observe a larger portion of the uncaptured beam being at lower energy with respect to the main bunches [Fig. 14(d)(A)]. The rate at which the particles drift away, defined by their energy deviation and the rf voltage, is well modeled in simulation. Furthermore, there is a small number of particles drifting away from the bunch train after the initial uncaptured beam, represented by the light blue color trailing behind the uncaptured beam [Fig. 14(d)(B)]. These particles can also be observed in the measurement.

The particles entering the frame of the FBCT at the start of the turn at around 1 s into the cycle are the ones that left the frame at the end of the turn, due to the periodic boundary conditions at the start and end of the turn. The tracking code BLonD is able to model such boundary conditions and one can observe these particles in Fig. 14(d) as well.

The main difference between measurement and simulation occurs one second after the injection. Here, the distribution of drifting particles disperses more along the turn in the simulation compared to the measurement. The timescale is of the order of seconds while the synchrotron period is 1.5 ms. Hence, small differences in the initial momentum distribution of the uncaptured beam can lead to large differences in arrival time of the particles over such timescales. A likely explanation for this is therefore a small difference in the distribution of momentum deviation in simulation and measurement. Another reason could be that the FBCT is not able to accurately resolve the population at the head and tail of the uncaptured beam due to the relatively low number of particles.

D. Reproducing losses at the start of the ramp in the SPS

During the first 200 ms after injection, the total uncaptured beam intensity was found by computing the difference between the direct current (dc) BCT, which detects the total beam intensity, and the FBCT [26]. Furthermore, the beam losses at the start of the ramp were estimated from the dc BCT by computing the step in total beam intensity at the start of the SPS acceleration ramp, as depicted in Fig. 15 (dashed lines). These losses were then correlated with the injection phase offset from the BPL error at the turn it started acting (turn 5). The resulting losses plotted versus injection phase offset are summarized in Fig. 16.

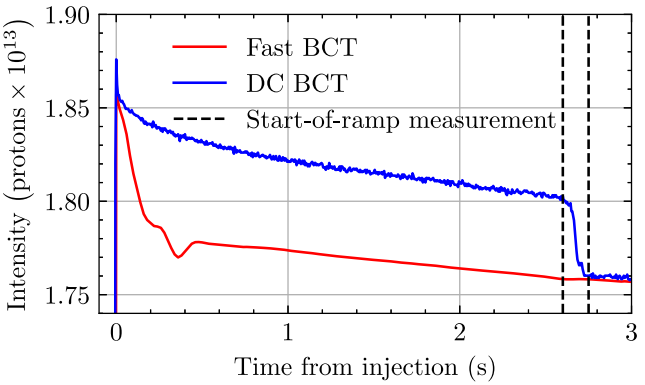

FIG. 15. Intensity evolution measured by the FBCT (red) and the dc BCT (blue). The dashed black lines indicate the part of the cycle from which the start-of-ramp losses were estimated.

The estimated uncaptured beam and the start-of-ramp losses are closely connected. However, as bunches circulate at flat bottom, their emittance is blown up by intrabeam scattering (IBS) and noise of the rf system. These processes will slowly push particles out of the rf buckets and therefore give additional contributions to the losses at the start of the

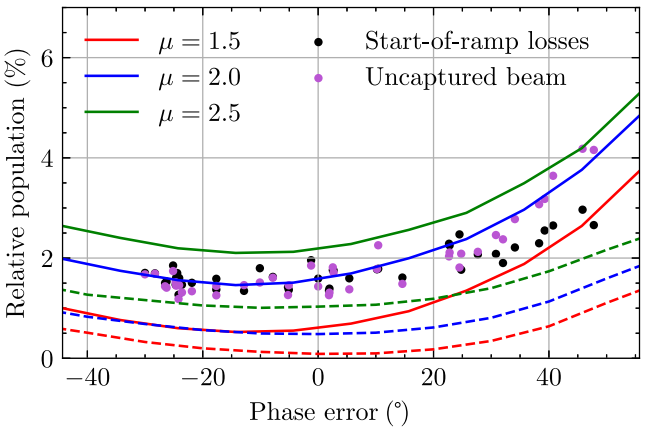

FIG. 16. Simulated uncaptured beam for different injection offsets (lines) plotted with the estimated start-of-ramp losses (black) and uncaptured beam (purple) from measurement. The red, blue, and green lines are simulations for bunch profiles with a binomial μ of 1.5, 2.0, and 2.5, respectively. The full lines are losses from simulation using the dynamic CC model and dashed lines from simulations with a simplified effective impedance of the rf system.

ramp. The effect of rf noise and IBS has mostly been studied in detail for ion beams in the SPS [46,47]. Due to the lower particle charge with protons, IBS-induced debunching is expected to be smaller. Furthermore, the studies in [46,47] were performed before the upgrade of the SPS low-level rf (LLRF) system [48]. The contribution from rf noise is therefore expected to be reduced as well. As a check, the bunch length evolution measured by the SPS beam quality monitor was analyzed to verify that these effects could be neglected. Indeed, the average bunch length near the start of the ramp was found to be equal to the filamented bunch length after injection, within a 2% spread. There was therefore likely very little debunching during the 2.6 s long flat bottom, which consequently gave a negligible contribution to the start-of-ramp losses. Hence, the losses at the start of the ramp were dominated by uncaptured beam during the cycle.

Scans in injection phase offsets were also performed with the simulation model for SPS injection. For each simulation, the uncaptured beam was estimated by counting the macroparticles outside the rf buckets after 1500 turns. This simulated uncaptured beam is also plotted in Fig. 16. Two sets of simulations were performed, one set with the dynamic model of the CC in the SPS and the other with the simplified model. In addition, three different beam distributions were simulated using binomial exponents of 1.5, 2.0, and 2.5 to modify the tail content at injection.

As one would intuitively expect, Fig. 16 shows that the measured losses increase for higher phase offsets. The simulations using the dynamic rf system model reproduce these characteristics of the losses closely both in dependence versus phase error and in absolute value. In comparison, the simplified model underestimates the losses by a factor of two. Furthermore, comparing the three different binomial bunch profiles, the beam distribution with an exponent of 2.0 matches the data the best, indicating possible larger tails in reality than can be measured in the PS. For phase offsets larger than 35°, the estimated start-of-ramp losses and the uncaptured beam from the measurements diverge. Only the measured uncaptured beam matches the estimates from the simulations using $\mu = 2.0$ for these phase errors. The difference between the uncaptured beam and start-of-ramp losses is likely caused by the large phase errors producing more uncaptured particles at higher momentum offsets. These particles will therefore hit the momentum aperture of the SPS before the acceleration ramp.

VII. CONCLUSIONS

A self-consistent coupling of local and global rf feedback models has been implemented in the macroparticle simulation code BLonD. This has enabled the most accurate model so far of the complex longitudinal beam behavior at injection with strong intensity effects. Benchmarks against measurements in the SPS and LHC show how the local feedback models in BLonD closely reproduce important observables of both the beam and the rf system. Simulations with momentum offsets in the SPS demonstrate that the local LLRF feedback models are correctly decoupled from the design reference frame and follow the rest of the rf system. Furthermore, simulations of injection into the LHC show the correct dynamics when converging to steady state. The test also shows the consistency of the beam phase relative to the rf phase between the BPL and the CC.

Measurements of injection transients were analyzed in the SPS and reproduced with high accuracy using the coupled rf system model. The simulations show excellent agreement with measurements of the beam filamenting after injection including offsets in both phase and energy. Furthermore, the measurements of the uncaptured beam after injection and how these particles continue to circulate off-momentum at the flat bottom closely agree with simulation. Finally, the beam losses at the start of the ramp versus injection phase error predicted by the simulations match what was found during the measurements. This shows that the BLonD model is able to correctly combine the changing phase due to the BPL, the transient beam loading from the CC model, and the intensity effects from the beam-coupling impedance.

The evolved simulation models in BLonD, combining both the beam control and the CC in the SPS and LHC, are also essential tools to study the bunch-to-bucket transfer into the LHC. In the HL-LHC era, reducing the uncaptured beam generated at injection will be a challenge due to the stringent limitations in rf power. The presented simulation models are now extensively being applied to make projections for HL-LHC and to study mitigation techniques. The newly developed infrastructure in the BLonD simulation suite related to control loops, including the generic methods described in this paper, is also applicable beyond the concrete SPS and LHC cases. The flexible implementation can easily be extended and applied to other synchrotrons to investigate the complex longitudinal dynamics in transient regimes, such as at injection. As a next step, for instance, the BLonD infrastructure will be applied for modeling the CC driving the HL-LHC crab cavities, which is currently being refined. Using an appropriate model of the transverse dynamics, these simulations will mainly be used to study longitudinal dynamics with the crab cavity CC. For the design of future accelerators, the modeling framework in BLonD can moreover enable us to obtain relevant beam dynamics based input already at an early stage in the development of new rf feedback systems. For the Future Circular Collider, it is foreseen to include beam-related aspects from the beginning by conceiving and optimizing the LLRF system with models in simulation tools like BLonD.

ACKNOWLEDGMENTS

We would like to thank D. Barrientos, R. Calaga, H. Damerau, and M. Zampetakis for fruitful discussions as well as F. Gerigk, B. Goddard, and M. Zerlauth for useful comments on the manuscript. Support for the machine development studies from the PS and SPS shift crews is gratefully acknowledged. This research is supported by the HL-LHC project.

DATA AVAILABILITY

The data that support the findings of this article are not publicly available upon publication because it is not technically feasible and/or the cost of preparing, depositing, and hosting the data would be prohibitive within the terms of this research project. The data are available from the authors upon reasonable request.

APPENDIX: EXECUTION TIMES OF THE SIMULATIONS

The execution time of the simulations presented in this paper is summarized in Table VI. The BLonD suite was compiled with OpenMP [49] and the simulations were all run on an Apple M4 Pro CPU with 12 cores and 24 GB of RAM. Notice that the simulations in Secs. V A and V B were executed without beam-induced voltages except for the ones calculated by the CC model. The fraction of the runtime used for beam-induced voltage calculations is therefore left out in the table for these simulation cases.

Tracking of the CC models takes up most of the runtime for the simulations without any other intensity effects. However, for the simulations in Secs. III A, III B, and VI, the time spent tracking the CC models is comparable to the macroparticle tracking and the other induced voltage calculations.

TABLE VI. Execution times for the simulations presented in the paper. The variable N_{macro} is the total number of macroparticles in the simulation, N_{bins} is the number of samples of the beam line density, t_{bins} is the sampling period of the line density, and N_{turns} is the number of turns simulated. The runtime of the simulation is t_{sim} while the last five columns are the percentage of the runtime spent for the different simulation elements. The time spent performing the kicks and drifts on the macroparticles is r_{track}, r_{profile} is the time to update the line density, r_{ind} is the time to calculate the induced voltage, r_{CC} is the time to track the CC, and r_{other} is the time spent for other operations, e.g., storing turn-by-turn data.

Simulation	N_{macro}	N_{bins}	t_{bins} (ps)	N_{turns}	t_{sim} (s)	r_{track} (%)	r_{profile} (%)	r_{ind} (%)	r_{CC} (%)	r_{other} (%)
Section III A—SPS flattop	4.4×10^7	1.0×10^5	39	10 000	518	20	12	14	50	4
Section III B—LHC flat bottom	5.6×10^{7}[a]	5.2×10^5	19	300	98	2	1	18	77	2
Section V A—SPS flattop	3.6×10^6	1.5×10^5	39	10 000	702	2	5	⋯	88	5
Section V B—LHC flat bottom	3.6×10^6	1.2×10^4	78	2000	267	0.8	0.5	⋯	98	0.7
Section VI—SPS flat bottom	7.2×10^7	4.9×10^4	39	1500	67	36	19	13	28	4

[a]The number of macroparticles changed from 1.2×10^7 to the final amount during the runtime of the simulation to model the 12 bunches already circulating and the injection of the 36-bunch train.

[1] D. Boussard, Design of a ring rf system, Technical Report No. CERN-SL-91-02-RFS, CERN, 1991.

[2] U. Bigliani, The beam control system for the CERN PS booster, IEEE Trans. Nucl. Sci. **18**, 352 (1971).

[3] J. M. Brennan, RF beam control for the AGS booster, Technical Reports No. BNL-52438, AGS/AD-94-6, Brookhaven National Laboratory, 1994.

[4] P. Baudrenghien, G. Hagmann, J. C. Molendijk, R. Olsen, A. Rohlev, V. Rossi, D. Stellfeld, D. Valuch, and U. Wehrle, The LHC low level rf, in *Proceedings of the 10th European Particle Accelerator Conference, Edinburgh, United Kingdom* (JACoW, Geneva, Switzerland, 2006).

[5] J. Grieser, J. Adamy, T. Ferrand, K. Gross, U. Hartel, H. Klingbeil, U. Laier, D. Lens, K.-P. Ningel, S. Schäfer, and B. Zipfel, A digital beam-phase control system for a heavy-ion synchrotron with a dual-harmonic cavity system, IEEE Trans. Nucl. Sci. **61**, 3584 (2014).

[6] E. Cullerton, B. Schupbach, B. Pellico, B. Chase, P. Varghese, and D. Klepec, Fermilab PIP-II booster LLRF upgrade, Technical Report No. FERMILAB-CONF-19-530-AD-PIP2, Fermi National Accelerator Laboratory (FNAL), Batavia, IL, 2018.

[7] A. Spierer, P. Baudrenghien, J. Egli, G. Hagmann, P. Kuzmanović, I. Stachon, M. Sumiński, and T. Włostowski, The CERN SPS low level rf: The beam-control, in *Proceedings of the 13th International Particle Accelerator Conference, Bangkok, Thailand* (JACoW, Geneva, Switzerland, 2022), 10.18429/JACoW-IPAC2022-TUPOST021.

[8] O. Naumenko and A. Lasheen, Modelling of the PS beam phase and radial feedback loops, Technical Report No. CERN-ACC-NOTE-2024-0011, CERN, 2024.

[9] A. Gamp, J. Kibinski, A. Millhouse, M. Schweiger, and H. J. Stuckenberg, Damping of coherent synchrotron oscillations occuring at injection of 7.5 GeV protons into

PETRA II, in *Proceedings of the 2nd European Particle Accelerator Conference, Nice, France* (Ed. Frontieres, Gif-sur-Yvette, France, 1990).

[10] T. Mastoridis, P. Baudrenghien, A. Butterworth, J. Molendijk, C. Rivetta, and J. D. Fox, Radio frequency noise effects on the CERN Large Hadron Collider beam diffusion, Phys. Rev. ST Accel. Beams **14**, 092802 (2011).

[11] P. Baudrenghien, A. Butterworth, M. Jaussi, T. Mastoridis, G. Papotti, and E. Shaposhnikova, Longitudinal emittance blow-up in the LHC, in *Proceedings of the 2nd International Particle Accelerator Conference, San Sebastián, Spain* (JACoW, Geneva, Switzerland, 2011).

[12] K. Meisner, RF synchronous transfer into specific buckets between Fermilab main ring and Tevatron accelerators, in *Proceedings of the 15th IEEE Particle Accelerator Conference, Washington, DC, USA* (IEEE, Piscataway, NJ, 1993).

[13] P. L. Corredoura, L. Sapozhnikov, and R. Tighe, RF feedback development for the PEP-II B factory, in *Proceedings of the 4th European Particle Accelerator Conference, London, United Kingdom* (World Scientific, Singapore, 1994).

[14] K. Akai, E. Ezura, and S. Yashimoto, Experiment of rf feedback using an improved parallel comb-filter, in *Proceedings of the 5th European Particle Accelerator Conference, Sitges, Spain* (IOP, Bristol, 1996).

[15] P. Baudrenghien and T. Mastoridis, Fundamental cavity impedance and longitudinal coupled-bunch instabilities at the High Luminosity Large Hadron Collider, Phys. Rev. Accel. Beams **20**, 011004 (2017).

[16] T. Mastoridis and P. Baudrenghien, CERN's super proton synchrotron 200 MHz cavity regulation upgrade: Modeling, design optimization, and performance estimation, Phys. Rev. Accel. Beams **25**, 021002 (2022).

[17] G. Iadarola *et al.*, Xsuite: An integrated beam physics simulation framework, in *Proceedings of the 68th Advanced Beam Dynamics Workshop High-Intensity High-Brightness Hadron Beams, Geneva, Switzerland* (JACoW, Geneva, Switzerland, 2024).

[18] R. De Maria *et al.*, SixTrack version 5: Status and new developments, in *Proceedings of the 10th International Particle Accelerator Conference, Melbourne, Australia* (2019).

[19] A. Gamelin, W. Foosang, and R. Nagaoka, MBTRACK2, a collective effect library in Python, in *Proceedings of the 12th International Particle Accelerator Conference, Campinas, SP, Brazil* (JACoW, Geneva, Switzerland, 2021).

[20] M. Borland, ELEGANT: A flexible SDDS-compliant code for accelerator simulation, in *Proceedings of the 6th International Computational Accelerator Physics Conference, Darmstadt, Germany* (GSI, Darmstadt, 2000).

[21] M. Zampetakis, T. Argyropoulos, Y. Brischetto, R. Calaga, L. Giacomel, B. E. Karlsen-Baeck, I. Karpov, N. Mounet, B. Salvant, and H. Timko, Refining the LHC longitudinal impedance model, in *Proceedings of the 68th Advanced Beam Dynamics Workshop High-intensity High-brightness Hadron Beams, Geneva, Switzerland* (JACoW, Geneva, Switzerland, 2023).

[22] D. Quartullo, L. Intelisano, I. Karpov, and G. Papotti, Simulation studies of longitudinal stability for high-intensity LHC-type beams in the CERN SPS, in *Proceedings of the 13th International Particle Accelerator Conference, Bangkok, Thailand* (JACoW, Geneva, Switzerland, 2022).

[23] O. S. Brüning, P. Collier, P. Lebrun, S. Myers, R. Ostojic, J. Poole, and P. Proudlock, *LHC Design Report, CERN Yellow Reports: Monographs* (CERN, Geneva, 2004).

[24] O. Aberle *et al.*, *High-Luminosity Large Hadron Collider (HL-LHC): Technical Design Report*, CERN Yellow Reports: Monographs (CERN, Geneva, 2020).

[25] H. Timko, T. Argyropoulos, R. Calaga, N. Catalan Lasheras, K. Iliakis, B. E. Karlsen-Baeck, I. Karpov, and M. Zampetakis, Advances on LHC rf power limitation studies at injection, in *Proceedings of the 68th Advanced Beam Dynamics Workshop High-intensity High-brightness Hadron Beams, Geneva, Switzerland* (JACoW, Geneva, Switzerland, 2023).

[26] B. E. Karlsen-Bæck, B. Salvachua, H. Timko, M. Zampetakis, and S. Morales Vigo, Correlating start-of-ramp losses with beam observables at flat-bottom in the LHC, in *Proceedings of the 15th International Particle Accelerator Conference, Nashville, TN, USA* (JACoW, Geneva, Switzerland, 2024).

[27] M. Schwarz, H. Bartosik, A. Lasheen, J. Repond, E. Shaposhnikova, and H. Timko, Studies of capture and flat-bottom losses in the SPS, in *Proceedings of the 61st ICFA ABDW on High-intensity and High-brightness Hadron Beams, Daejeon, Korea* (JACoW, Geneva, Switzerland, 2018).

[28] H. Timko, S. Albright, T. Argyropoulos, H. Damerau, K. Iliakis, L. Intelisano, B. E. Karlsen-Baeck, I. Karpov, A. Lasheen, L. Medina, D. Quartullo, J. Repond, A. L. Vanel, J. E. Müller, M. Schwarz, P. Tsapatsaris, and G. Typaldos, Beam longitudinal dynamics simulation studies, Phys. Rev. Accel. Beams **26**, 114602 (2023).

[29] H. Timko, J. Esteban Müller, A. Lasheen, and D. Quartullo, Benchmarking the beam longitudinal dynamics code BLonD, in *Proceedings of the 7th International Particle Accelerator Conference, Busan, Korea* (JACoW, Geneva, Switzerland, 2016).

[30] B. E. Karlsen-Baeck. Modelling control loops for SPS-LHC beam transfer studies, Master's thesis, Norwegian University of Science and Technology, 2022.

[31] B. E. Karlsen-Bæck, T. Argyropoulos, R. Calaga, I. Karpov, and H. Timko, Validation of control loop modeling for power limitation studies with beams for HL-LHC, in *Proceedings of the 14th International Particle Accelerator Conference, Venice, Italy* (JACoW, Geneva, Switzerland, 2023).

[32] P. Corredoura, Architecture and performance of the PEP-II low-level rf system, in *Proceedings of the 18th IEEE Particle Accelerator Conference, New York, NY, USA* (IEEE Computer Society Press, Piscataway, NJ, 1999).

[33] G. Hagmann, P. Baudrenghien, J. Egli, A. Spierer, M. Suminski, and T. Wlostowski, The CERN SPS low level rf: The cavity-controller, in *Proceedings of the 13th International Particle Accelerator Conference, Bangkok, Thailand* (JACoW, Geneva, Switzerland, 2022).

[34] J. Tückmantel, Cavity-beam-transmitter interaction formula collection with derivation, Technical Report No. CERN-ATS-Note-2011-002 TECH, CERN, 2010.

[35] G. Dôme, The SPS acceleration system travelling wave drift-tube structure for the CERN SPS, in *Proceedings of the 9th Linear Accelerator Conference, Chalk River, Canada* (A.E.C.L., Chalk River, 1976).

[36] J. Holma, The model and simulations of the LHC 400 MHz cavity controller, Technical Report No. CERN-AB-Note-2007-012, CERN, 2007.

[37] P. Baudrenghien and T. Mastoridis, I/Q model of the SPS 200 MHz travelling wave cavity and feedforward design, Technical Report No. CERN-ACC-NOTE-2020-0032, CERN, 2020.

[38] J. Coupard *et al.*, LHC injectors upgrade, technical design report—volume 1: Protons, Technical Report No. CERN-ACC-2014-0337, CERN, 2014.

[39] R. Garoby, A non-adiabatic procedure in the PS to supply the nominal proton bunches for LHC into 200 MHz RF buckets in SPS, Technical Report No. CERN-PS-RF-Note-93-17, CERN, 1993.

[40] H. Timko, T. Argyropoulos, T. Bohl, H. Damerau, J. F. Esteban Müller, S. Hancock, and E. Shaposhnikova, Longitudinal transfer of rotated bunches in the CERN injectors, Phys. Rev. ST Accel. Beams **16**, 051004 (2013).

[41] J. L. Laclare, Bunched beam coherent instabilities, in *Proceedings of the CAS 1985, Oxford, United Kingdom* (CERN, Geneva, Switzerland, 1987).

[42] A. Lasheen, T. Argyropoulos, T. Bohl, J. F. Esteban Müller, H. Timko, and E. Shaposhnikova, Beam measurement of the high frequency impedance sources with long bunches in the CERN Super Proton Synchrotron, Phys. Rev. Accel. Beams **21**, 034401 (2018).

[43] L. Intelisano, H. Damerau, and I. Karpov, Threshold for loss of Landau damping in double-harmonic rf systems, Phys. Rev. Accel. Beams **28**, 104402 (2025).

[44] D. Quartullo, S. Albright, H. Damerau, A. Lasheen, G. Papotti, and C. Zisou, RF voltage calibration using phase space tomography in the CERN SPS, in *Proceedings of the 13th International Particle Accelerator Conference, Bangkok, Thailand* (JACoW, Geneva, Switzerland, 2022).

[45] A. Lasheen, H. Damerau, I. Karpov, G. Papotti, and E. Vinten, Longitudinal collective effects at beam transfer from PS to SPS at CERN, in *Proceedings of the 68th Advanced Beam Dynamics Workshop High-Intensity High-Brightness Hadron Beams* (JACoW, Geneva, Switzerland, 2023).

[46] F. Antoniou, H. Bartosik, A. Huschauer, and A. Saa Hernandez, Transverse studies with ions at SPS flat bottom. in *Proceedings of the Injector MD Days* (CERN, Geneva, Switzerland, 2017).

[47] A. Saa Hernandez, F. Antoniuo, H. Bartosik, and A. Huschauer, Characterization of losses and emittance growth for ion beams on the SPS injection plateau, in *Proceedings of the 9th International Particle Accelerator Conference, Vancouver, BC, Canada* (JACoW, Geneva, Switzerland, 2018).

[48] G. Hagmann, P. Baudrenghien, J. D. Betz, J. Egli, G. Kotzian, M. Rizzi, L. Schmid, A. Spierer, T. Wlostowski, and F. J. Galindo Guarch, The CERN SPS low level rf upgrade project, in *Proceedings of the 10th International Particle Accelerator Conference, Melbourne, Australia* (JACoW, Geneva, Switzerland, 2019).

[49] K. Iliakis, H. Timko, S. Xydis, and D. Soudris, BLonD++: Performance analysis and optimizations for enabling complex, accurate and fast beam dynamics studies, in *Proceedings of the 18th International Conference on Embedded Computer Systems: Architectures, Modeling, and Simulations, Pythagorion, Greece* (ACM, New York, NY, 2018).